Shapes of a Suspended Curly Hair

J. t. Miller, Arnaud Lazarus, Basile Audoly, P. m. Reis

Shapes of a Suspended Curly Hair

J. T. Miller,[1] A. Lazarus,[2] B. Audoly,[3] and P. M. Reis[1,2,*]

[1]*Department of Civil & Environmental Engineering, Massachusetts Institute of Technology, Cambridge, Massachusetts 02139, USA*
[2]*Department of Mechanical Engineering, Massachusetts Institute of Technology, Cambridge, Massachusetts 02139, USA*
[3]*Sorbonne Universités, UPMC Univ Paris 06, CNRS, UMR 7190 Institut Jean Le Rond d'Alembert, F-75005 Paris, France*

We investigate how natural curvature affects the configuration of a thin elastic rod suspended under its own weight, as when a single strand of hair hangs under gravity. We combine precision desktop experiments, numerics, and theoretical analysis to explore the equilibrium shapes set by the coupled effects of elasticity, natural curvature, nonlinear geometry, and gravity. A phase diagram is constructed in terms of the control parameters of the system, namely the dimensionless curvature and weight, where we identify three distinct regions: planar curls, localized helices, and global helices. We analyze the stability of planar configurations, and describe the localization of helical patterns for long rods, near their free end. The observed shapes and their associated phase boundaries are then rationalized based on the underlying physical ingredients.

Hairstyle has a marked effect on a person's appearance, for whom hair color, length, and curliness can all be distinguishing characteristics. The bulk appearance of a head of hair, in particular, is governed by the shape of the individual strands and their collisions [1]. This topic is of great importance to the computer animation industry [2] to achieve visually realistic representations. Curly hair can also be taken as an analogue for other instances of naturally curved filamentary structures that abound in nature and technology. These include DNA [3], plant tendrils [4], and pipes and cables [5], all of which can display similar behavior across widely different length scales. Given their extreme slenderness, these rodlike structures can undergo large rotations while remaining in the small strain regime, and are amenable to a unified framework that couples linear elasticity and nonlinear geometry. In the absence of natural curvature, the nonlinear equilibrium equations for rods are integrable thanks to Kirchhoff's analogy with the motion of a spinning top [6]. For naturally curved rods, however, existing explicit solutions are essentially limited to helices [7,8], which require the external load to be highly symmetric. We have recently found that natural curvature can dramatically affect the mechanical behavior of rods [9], both quantitatively and qualitatively. There is, therefore, a need to develop a predictive framework that is applicable to naturally curved rods subjected to a nonsymmetric load, which can result in spatially heterogeneous configurations.

Here, we explore the deceivingly simple problem of predicting the shape of a naturally curved rod that is clamped and suspended under its own weight, which we take to be a representative metaphor of a curly hair. To tackle this, we perform a combination of precision model experiments, simulations, and theoretical analysis. In Fig. 1, we present examples of five rods with increasing values of their stress-free natural curvature κ_n, but that are otherwise identical in all other mechanical properties. Our experimental fabrication protocol allows for a fine control of κ_n, which we therefore take as an independent control parameter. If the rod is naturally straight [e.g., Fig. 1(a) for $\kappa_n = 0$] it hangs vertically. For small values of κ_n, the configurations are planar [e.g., Figs. 1(b) and 1(c) for $\kappa_n = 6$ and 38 m^{-1}, respectively]; the rods are straight near their clamp but develop a curled hook near their free end. As κ_n is progressively increased, this hook looses stability and the rod acquires a nonplanar three-dimensional shape. A curl first localizes near the free end [e.g., Fig. 1(d) for $\kappa_n = 56$ m^{-1}] and global helical configurations are obtained for high values of κ_n [e.g., Fig. 1(e) for $\kappa_n = 62$ m^{-1}]. We focus on rationalizing how these shapes are set by the balance between elasticity, geometry, and

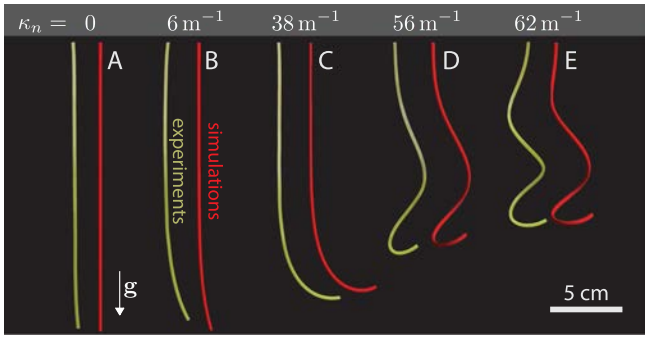

FIG. 1 (color online). Equilibrium shapes of rods suspended under their own weight: comparison of experiments and simulations. The natural curvature κ_n is varied, while the length $L = 20$ cm, radius $r = 1.55$ mm, elasticity parameters ($E = 1290$ kPa, $\nu = 0.5$), and volumetric mass $\rho = 1200$ kg/m^3 are kept constant.

gravity. Our approach is complementary to Ref. [1], where collisions within an ensemble of hair were treated using a statistical mechanics approach to describe the overall bulk shape of a ponytail. Taking an alternative point of departure, we identify the transitions between planar and nonplanar shapes for an analogue of a single curly hair and describe the nonplanar shapes in detail.

In our experiments, we custom fabricate rods by injecting vinylpolysiloxane into a flexible polyvinyl chloride (PVC) tube, whose inner diameter sets the radius of the rod, $r = 1.55$ mm. The PVC tube is wound around a cylindrical object (or laid straight), which sets a constant (or infinite) radius of curvature on the rod upon subsequent curing and demolding [9]. Our fabrication procedure allows for the precise control of the natural curvature in the range $0 < \kappa_n\ [\mathrm{m}^{-1}] < 62$, a parameter that we vary systematically. For helically and tightly wound PVC tubes, this fabrication procedure creates a constant nonzero but small natural twist, which we neglect. The Young's modulus of the elastomer is measured to be $E = 1290 \pm 12$ kPa, the Poisson ratio is $\nu \approx 0.5$, and the volumetric mass is $\rho = 1200\ \mathrm{kg/m^3}$. Each experimental test consists of mounting a single rod with suspended length in the range $1 < L\ [\mathrm{cm}] < 20$ onto a clamp that is aligned vertically. The rod is then suspended under its own weight and allowed to reach static equilibrium, as shown in Fig. 1 (green configurations). Three-dimensional reconstructions of the rods are produced by taking digital images from two perpendicular directions and performing image processing to obtain their centerlines.

We also perform numerical simulations, representative examples of which are presented in Fig. 1 (red configurations), where all parameters match those of the experiments. Good agreement is found throughout between the two. The simulations compute the equilibria of an inextensible three-dimensional elastica subjected to its own distributed weight, and account for both bending and twisting. The numerical method was developed using the continuation software package MANLAB [10] and is described in detail in Ref. [9].

Our first quantitative test is provided by comparing the experimentally measured and simulated vertical elevation of the tip, h, between the clamp and the free end of the rod. In Fig. 2 we plot h as a function of the total arc length L for three values of the natural curvature κ_n. Quantitative agreement is found between experiments (data points) and simulations (solid lines). For the two lowest values of $\kappa_n = 16.6$ and $38\ \mathrm{m}^{-1}$, the configurations are planar for all lengths tested and h decreases monotonically with L. For $\kappa_n = 56.2\ \mathrm{m}^{-1}$, however, planar shapes are observed for $L \lesssim 0.1$ m [see Figs. 2(f) and 2(g)] but nonplanar ones are observed for $L \gtrsim 0.1$ m [see Figs. 2(h) and 2(i)].

With the aim of rationalizing the behavior observed in both the experiments and simulations, we use an inextensible rod model with natural curvature [11]. All lengths are

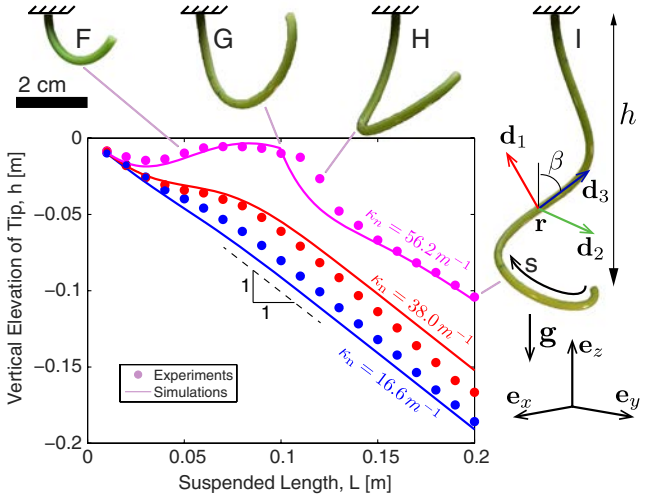

FIG. 2 (color online). Vertical elevation of the tip h versus arc length of the rod L, for three different natural curvatures $\kappa_n = (16.6, 38.0, 56.2)\ \mathrm{m}^{-1}$: experiments (circles) and simulations (solid lines). For $\kappa_n = 56.2\ \mathrm{m}^{-1}$, the configurations F and G are planar while the configurations H and I are nonplanar.

rescaled by the natural radius of curvature, κ_n^{-1}. For example, $\bar{s} = s\kappa_n$ denotes the rescaled arc length, $0 \le \bar{s} \le \bar{L}$, with its origin at the free end, $\bar{s} = 0$. The dimensionless length $\bar{L} = \kappa_n L$ offers a measure of the rod's curliness. All energies are rescaled by $B\kappa_n$, where $B = EI$ and $I = \pi r^4/4$ are the bending stiffness and area moment of inertia of the rod, respectively.

The configurations are defined in terms of the position of its centerline $\bar{\mathbf{r}}(\bar{s})$, and an orthonormal director basis $(\mathbf{d}_1(\bar{s}), \mathbf{d}_2(\bar{s}), \mathbf{d}_3(\bar{s}))$, subjected to the condition $\bar{\mathbf{r}}' = \mathbf{d}_3$, with primes denoting derivation with respect to $\bar{s}$. The Cartesian basis $\mathbf{e}_i$ is chosen such that the clamping condition writes $\bar{\mathbf{r}}(\bar{L}) = \mathbf{0}$ and $(\mathbf{d}_1, \mathbf{d}_2, \mathbf{d}_3)_{\bar{s}=\bar{L}} = (\mathbf{e}_y, -\mathbf{e}_x, \mathbf{e}_z)$. The material curvatures $\bar{\kappa}_1$ and $\bar{\kappa}_2$ and twist $\bar{\kappa}_3$ are defined by $\bar{\kappa}_i = \frac{1}{2}\epsilon_{ijk}\mathbf{d}_j' \cdot \mathbf{d}_k$, where ϵ_{ijk} is the skew-symmetric permutation tensor $\epsilon_{ijk} = (\mathbf{e}_i \times \mathbf{e}_j) \cdot \mathbf{e}_k$. The total energy of the rod is then written as

$$\bar{\mathcal{E}} = \int_0^{\bar{L}} \left(\frac{1}{2}[(\bar{\kappa}_1 - 1)^2 + \bar{\kappa}_2{}^2 + \bar{C}\bar{\kappa}_3{}^2] - \bar{w}\,\bar{s}\cos\beta \right) d\bar{s}, \quad (1)$$

where $\bar{C}$ is the ratio between the twisting and bending moduli and $\bar{w} = w/B\kappa_n^3$ is the dimensionless weight. The weight per unit length for a rod with circular cross section is $w = \rho\pi r^2 g$ in physical units, g being the acceleration of gravity. We set $\bar{C}(\nu) = (1+\nu)^{-1} = 2/3$ since our rods are cylindrical and $\nu \approx 0.5$. Finally, β is the angle between the tangent $\mathbf{d}_3$ and the vertical, such that $\cos\beta = \mathbf{d}_3 \cdot \mathbf{e}_z$, as illustrated in the schematic of Fig. 2. The first term in the integrand of Eq. (1) represents the strain energy and $\frac{1}{2}(\bar{\kappa}_1 - 1)^2$ considers the natural curvature, which is unity in this dimensionless description. The second term in the integrand corresponds to the gravitational potential energy.

The control parameters of the curly rods are therefore their dimensionless length $\bar{L}$ and weight $\bar{w}$.

Our simulations compute the stationary points of the energy in Eq. (1) for fixed values of $\bar{L}$ and $\bar{w}$. In Fig. 3, we present the phase diagram of the system in the ($\bar{L}$, $\bar{w}$) parameter space, which is explored systematically. The numerical results (shaded regions) were obtained by simulating 11 110 equilibrium shapes within the following ranges of physical properties: Young's modulus $96 < E$ [kPa] < 9600, length $5 < L$ [cm] < 50, and natural curvature $0 < \kappa_n$ [m^{-1}] < 100. For a direct comparison, in Fig. 3 we also superpose the results of 170 experiments in the ranges $0 < L$ [cm] < 52 and $0 < \kappa_n$ [m^{-1}] < 65, while keeping $E = 1290$ kPa constant.

The shapes can be classified as (i) planar, (ii) nonplanar localized helical, and (iii) nonplanar global helical, representative examples of which are presented in Figs. 3(j)–3(l), respectively. The localized helices, in particular, consist of a helical portion near the free end, underneath a vertical and straight section closer to the clamp (our threshold for a straight section is $\beta \leq 1.5°$). A configuration is said to be a localized helix if the arc length of the helical portion is less that 95% of the total rod length and a global helix, otherwise. This classification protocol allows the smooth local-to-global transition to be represented by a curve in the phase diagram. The numerical and experimental configurations map onto the same regions of the phase diagram. We now seek to rationalize the boundaries between these regions.

The planar (2D) configurations of the suspended rod [e.g., Figs. 2(f) and 2(g)] can be recovered as a particular case of our general 3D model by setting $\bar{\kappa}_1 = \beta'$ and $\bar{\kappa}_2 = \bar{\kappa}_3 = 0$. These shapes have been solved analytically in Ref. [11] for various limits of $\bar{L}$ and $\bar{w}$. Here, we calculated them numerically by solving the nonlinear boundary-value problem for $\beta(\bar{s})$. Moreover, we have numerically computed their linear stability with respect to out-of-plane buckling, as a function of the parameters $\bar{w}$ and $\bar{L}$. The resulting curve of marginal stability has two asymptotes for $\bar{L} \gg 1$. The first corresponds to planar shapes consisting of a long, vertical tail connected to a hook near the free end. These configurations lose stability when the free end of the hook rises high enough to cause an overturning moment [e.g. Fig. 1(c)]. The corresponding buckling mode is localized near the free end and, as a result, the threshold $\bar{w}_c$ is independent of $\bar{L}$, for $\bar{L} \gg 1$. A detailed analysis yields $\bar{w}_c = 0.2391$ (for $\bar{L} = \infty$ and $\nu = 0.5$). This predicted boundary (thin vertical line between the blue and red regions in Fig. 3) is in excellent agreement with both the experiments and the simulations. The second asymptote for the transition between 2D and global (3D) helical shapes is observed to scale as $\bar{w}_c \sim \bar{L}^{-2}$, but a detailed analysis is beyond the scope of this study. These shapes correspond to 2D configurations involving self-contact, and have no direct counterpart in the experiments.

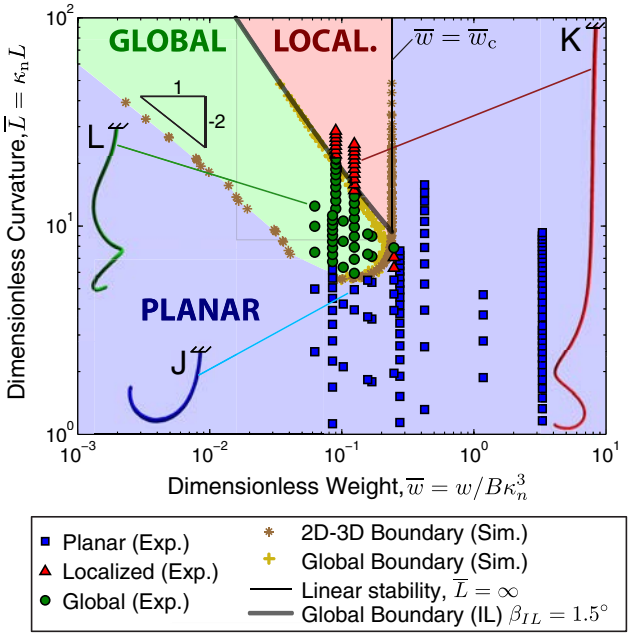

FIG. 3 (color online). Phase diagram for the rod configurations: planar (2D) and nonplanar (3D, global and localized helices). Each experimental data point is plotted on the ($\bar{L}$, $\bar{w}$) space, whereas only the phase boundaries are shown for the numerics. Theoretical curves for the planar-to-localized and localized-to-global transitions are superposed on the data. Three experimental reconstructions are shown as insets: (j) planar (blue, $\kappa_n = 49.5$ m^{-1}, $L = 10$ cm), (k) localized helix (red, $\kappa_n = 49.5$ m^{-1}, $L = 40$ cm), and (l) global helix (green, $\kappa_n = 62.3$ m^{-1}, $L = 20$ cm).

Having been able to predict the 2D-to-3D transition, we now focus on characterizing the helical configurations, with particular emphasis on long and curly rods, $\bar{L} \gg 1$. Since tension varies along the rod due to the distributed weight, the properties of the helices also evolve with arc length. Inspired by previous analyses of helices subjected to constant tension [8], we analyze these shapes assuming that the director $\mathbf{d}_2$ is perpendicular to the applied force (weight), such that $\mathbf{d}_2 \cdot \mathbf{e}_z \approx 0$ (as justified in the Supplemental Material [12] for a slowly varying tension). These configurations can be parametrized by the two Euler angles $\beta(\bar{s})$ and $\gamma(\bar{s})$ (shown schematically in Fig. 4), as $\mathbf{d}_1 = \cos\beta(-\sin\gamma\mathbf{e}_x + \cos\gamma\mathbf{e}_y) + \sin\beta\mathbf{e}_z$, $\mathbf{d}_2 = -\cos\gamma\mathbf{e}_x - \sin\gamma\mathbf{e}_y$ and $\mathbf{d}_3 = -\sin\beta(-\sin\gamma\mathbf{e}_x + \cos\gamma\mathbf{e}_y) + \cos\beta\mathbf{e}_z$. When the corresponding strains $\bar{\kappa}_1 = \gamma'\sin\beta$, $\bar{\kappa}_2 = -\beta'$, and $\bar{\kappa}_3 = \gamma'\cos\beta$ are inserted into the expression for the total energy in Eq. (1), we find that $\bar{\mathcal{E}}$ depends on γ' but not on γ, as a consequence of the cylindrical invariance about $\mathbf{e}_z$. Optimizing the resulting $\bar{\mathcal{E}}$ with respect to γ' yields $\gamma' = \kappa_n \sin\beta/\sin^2\beta + \bar{C}\cos^2\beta$ and, after eliminating γ', we obtain a reduced expression for the energy of helical shapes

$$\bar{\mathcal{E}}_{3D} = \int_0^{\bar{L}} \left(f(\bar{w}\,\bar{s}, \beta(\bar{s})) + \frac{1}{2}\beta'(\bar{s})^2 \right) d\bar{s}, \qquad (2)$$

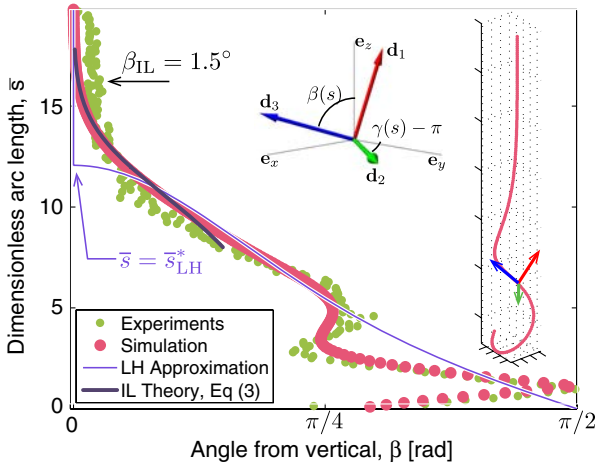

FIG. 4 (color online). A localized helical configuration as quantified by the angle from vertical, $\beta(\bar{s})$, for $\bar{L} = 19.8$ and $\bar{w} = 0.12$. Experimental and numerical results are compared to the predictions from the local helix (LH) and inner layer (IL) approximations described in the text. The arrows show the predicted position of the transition point for each approximation.

where $f(u,\beta) = \frac{1}{2}(1+\tan^2\beta/C)^{-1} - u\cos\beta$. The equilibrium configurations are stationary points of this energy with respect to $\beta(\bar{s})$. To compute them, we first introduce a local helix approximation, which we later refine by an inner layer theory.

In Fig. 4 we quantify a representative example of a localized curl in the limit of $\bar{L} \gg 1$ by measuring $\beta(\bar{s})$ from both the 3D experimental reconstructions and the numerical configurations, finding good agreement between the two. The rod is straight near the clamp, $\beta \approx 0$, while β increases in an oscillatory manner towards the free end at $\bar{s} = 0$. To analyze these localized shapes, we first assume that $\beta(\bar{s})$ varies slowly with $\bar{s}$, implying that the squared derivative in Eq. (2) can be neglected. We refer to this as the local helix (LH) approximation. The minimum energy is obtained by locally optimizing f with respect to β: $\partial f/\partial\beta = 0$. We recover the equation for the helical solutions of a spring subjected to constant tension [8]. It is known that the solution β of this implicit equation undergoes a pitchfork (symmetry-breaking) bifurcation as $\bar{w}\,\bar{s}$ is varied (purple curve in Fig. 4). The straight, vertical configuration, $\beta = 0$, is always an extremum of f, but it is unstable beyond $\bar{s}^*_{\rm LH} = (\bar{w}\,\bar{C})^{-1}$, where $\partial^2 f/\partial\beta^2 = \bar{w}\,\bar{s} - \bar{C}^{-1}$ becomes negative. For $\bar{s} \geq \bar{s}^*_{\rm LH}$, the upper part of the rod is subjected to a sufficiently large tension due to the weight of the portion underneath, causing it to remain vertical. On the other hand, for $0 \leq \bar{s} \leq \bar{s}^*_{\rm LH}$, the tension is low and the optimum value of β is nonzero, resulting in a helical configuration. This prediction captures the overall shape of the rod (purple curve in Fig. 4): the LH approximation agrees qualitatively with simulations and experiments even if it does not work well near the transition point, $\bar{s} = \bar{s}^*_{\rm LH}$, or near the free end, $\bar{s} = 0$.

In the vicinity of the transition point, $\bar{s} = \bar{s}^*_{\rm LH}$, the LH approximation fails because β varies quickly (see Fig. 4). Taking an alternative approach to the LH approximation above, we study this region using an inner layer (IL) approximation. The derivative $\beta'(\bar{s})$ is now restored in Eq. (2), and f is expanded near $\bar{s}^*_{\rm LH}$ for small β as $f \approx f_0 + \frac{1}{2}f_2\beta^2 + (1/24)f_4\beta^4$, where $f_2 = \partial^2 f/\partial\beta^2 = \bar{w}(\bar{s}-\bar{s}^*)$, and $f_4 = \partial^4 f/\partial\beta^4 = 3(4-3\bar{C}/\bar{C}^2)$. Dropping terms that are independent of β, we then have to minimize the functional $\int((\bar{w}(\bar{s}-\bar{s}^*)/2)\beta^2 + (f_4/24)\beta^4 + \frac{1}{2}\beta'^2)\,d\bar{s}$ within the inner layer. By the change of variable $S = \bar{s} - \bar{s}^*/\bar{w}^{-1/3}$ and unknown $B(S) = \sqrt{f_4/12}\bar{w}^{-1/3}\beta(\bar{s})$, the above functional can be rewritten as $\frac{1}{2}\int(SB^2 + B^4 + B'^2)\,dS$. The Euler-Lagrange condition yields the second Painlevé equation, $B''(S) = SB(S) + 2B^3(S)$. Interestingly, this equation arises in domains such as nonlinear optics, Bose-Einstein condensation, and random matrix theory [13]. It has a unique solution $B_{\rm HML}(S)$ connecting the symmetric solution $B \to 0$ for $S \to +\infty$ to the bifurcated solution $B \sim \sqrt{-S/2}$ for $S \to -\infty$, known as the Hastings-McLeod solution [14]. In terms of the original variables, the solution reads

$$\beta_{\rm IL}(\bar{s}) = \frac{2\bar{C}\bar{w}^{1/3}}{\sqrt{4-3\bar{C}}} B_{\rm HML}\left(\frac{\bar{s}-\bar{s}^*_{\rm LH}}{\bar{w}^{-1/3}}\right). \qquad (3)$$

This inner layer solution successfully describes the smooth transition between the helical and straight portions of rod near $\bar{s}^*_{\rm LH}$, as shown in Fig. 4.

Returning to the phase diagram of Fig. 3, we can now predict the transition from the localized to global helical configurations. With the same localization criterion used above, this phase boundary is expected to occur for $\beta_{\rm IL}(0.95\bar{L}) = 1.5°$ (thick gray curve in Fig. 3): this is in excellent agreement with the numerical and experimental results when the inner layer is indeed small, $\bar{L} \gg 1$, $\bar{w} \ll 1$ (see the Supplemental Material [12] for more details on the LH boundary). This, combined with our results above for the 2D-to-3D transition where a planar configuration becomes unstable, completes our rationalization of the phase diagram of Fig. 3.

Beyond a predictive description of the aesthetics of curly hair, our results can be directly applicable to a variety of engineering systems such as naturally curved fibers, wires, cables, and pipes. All of these rodlike structures are often manufactured, stored, and transported in spooled configurations, thereby imparting an intrinsic curvature, which can now be readily quantified using our framework as an inverse problem.

The authors wish to thank Y. Pomeau, J.-L. Lévêque, and B. Querleux for arousing our initial interest in hair mechanics, and B. Berry for her help with preliminary experiments. We are grateful for financial support from the National Science Foundation (CMMI-1129894), Schlumberger, the MIT-France Program, and the Battelle-MIT postdoctoral fellowship.

*preis@mit.edu

[1] R. E. Goldstein, P. B. Warren, and R. C. Ball, Phys. Rev. Lett. **108**, 078101 (2012).

[2] K. Ward, F. Bertails, T. Kim, S. Marschner, M. Cani, and M. Lin, IEEE Trans. Visual. Comput. Graph. **13**, 213 (2007).

[3] R. A. Mehta and J. D. Kahn, J. Mol. Biol. **294**, 67 (1999); L. M. Edelman, R. Cheong, and J. D. Kahn, Biophys. J. **84**, 1131 (2003); M. A. Morgan, K. Okamoto, J. D. Kahn, and D. S. English, Biophys. J. **89**, 2588 (2005).

[4] M. Raugh, *Some Geometry Problems Suggested by the Shapes of Tendrils* (Department of Mathematics, Stanford University, Stanford, CA, 1979); A. Goriely and M. Tabor, Phys. Rev. Lett. **80**, 1564 (1998).

[5] E. Zajac, J. Appl. Mech. **29**, 136 (1962); T. Yabuta, Bull. JSME **27**, 1821 (1984).

[6] G. Kirchhoff, J. Reine Angew. Math. **40**, 51 (1859); J. Coyne, IEEE Journal of Oceanic Engineering **15**, 72 (1990).

[7] A. Goriely and M. Tabor, Proc. R. Soc. A **453**, 2583 (1997); A. Champneys, G. Van der Heijden, and J. Thompson, Phil. Trans. R. Soc. A **355**, 2151 (1997).

[8] T. McMillen and A. Goriely, J. Nonlinear Sci. **12**, 241 (2002); N. Chouaieb, A. Goriely, and J. Maddocks, Proc. Natl. Acad. Sci. U.S.A. **103**, 9398 (2006).

[9] A. Lazarus, J. Miller, and P. Reis, J. Mech. Phys. Solids **61**, 1712 (2013); A. Lazarus, J. Miller, M. Metlitz, and P. Reis, Soft Matter **9**, 8274 (2013).

[10] S. Karkar, B. Cochelin, C. Vergez, O. Thomas, and A. Lazarus, *User Guide MANLAB 2.0* (2010).

[11] B. Audoly and Y. Pomeau, *Elasticity and Geometry: from Hair Curls to the Nonlinear Response of Shells* (Oxford University, New York, 2010).

[12] See Supplemental Material at http://link.aps.org/supplemental/10.1103/PhysRevLett.112.068103 for justification of kinematic assumption in the IL analysis and details on the transition predicted by the LH approximation.

[13] P. A. Clarkson, J. Comput. Appl. Math. **153**, 127 (2003); J. Giannini and R. Joseph, Phys. Lett. A **141**, 417 (1989); T. T. Wu, Phys. Rev. A **58**, 1465 (1998); C. A. Tracy and H. Widom, Commun. Math. Phys. **159**, 151 (1994).

[14] S. Hastings and J. McLeod, Arch. Ration. Mech. Anal. **73**, 31 (1980).